nature communications

Article

https://doi.org/10.1038/s41467-024-47058-1

# Supramolecular polynuclear clusters sustained cubic hydrogen bonded frameworks with octahedral cages for reversible photochromism

Received: 26 November 2023

Accepted: 18 March 2024

Published online: 30 March 2024

Check for updates

Xiaojun Ding[1], Jing Chen[1] & Gang Ye[1]

Developing supramolecular porous crystalline frameworks with tailor-made architectures from advanced secondary building units (SBUs) remains a pivotal challenge in reticular chemistry. Particularly for hydrogen-bonded organic frameworks (HOFs), construction of geometrical cavities through secondary units has been rarely achieved. Herein, a body-centered cubic HOF (TCA_$NH_4$) with octahedral cages was constructed by a $C_3$-symmetric building block and $NH_4^+$ node-assembled cluster $(NH_4)_4(COOH)_8(H_2O)_2$ that served as supramolecular secondary building units (SSBUs), akin to the polynuclear SBUs in reticular chemistry. Specifically, the octahedral cages could encapsulate four homogenous haloforms including $CHCl_3$, $CHBr_3$, and $CHI_3$ with truncated octahedron configuration. Crystallographic evidence revealed the cages served as spatially-confined nanoreactors, enabling fast, broadband photochromic effect associated with the reversible photo/thermal transformation between encapsulated $CHI_3$ and $I_2$. Overall, this work provides a strategy by shaping SSBUs to expand the framework topology of HOFs and a prototype of hydrogen-bonded nanoreactors to accommodate reversible photochromic reactions.

Construction of supramolecular porous structures with regular polyhedral architectures capturing guest molecules[1,2] offer opportunities for catalytic reaction[3,4], molecular recognition[5], and gas separation[6,7]. Most of the well-developed frameworks so far show open cavities with one or two-dimensional channels[8], lacking specific selectivity and dynamic sites for targeted objects[9,10]. Oppositely, synthesis of enclosed cavities with advanced symmetric three-dimensional cage architecture[11,12] or well-defined polyhedron[13] could implement efficient recognition and encapsulation of guest molecules[14,15]. At the same time, the isolated cavity could provide a potential platform and confined microenvironment for further physicochemical reactions[11,16].

For building sophisticated structures, nature gives representative examples to take advantage of secondary structures of proteins such as α-helix and β-sheet to assemble them into advanced living entities. There is no doubt that SBUs play important roles as nodes and clusters[17] in designing sophisticated substances[18]. The architectural and mechanical stability of metal-organic frameworks (MOFs) imparted by corresponding SBUs have given rise to unique framework chemistry. However, this concept has been rarely discussed in the design of HOFs with regular porosity, as HOFs are assembled by rigid building molecules through intermolecular hydrogen bonding[19–24]. Pristine hydrogen bonding interactions are too weak to stabilize rigid and directional polynuclear clusters[25–28]. The rational synthesis of porous HOFs with preorganized and highly symmetrical networks has been a long-term challenge[29]. Therefore, conventional hydrogen bonding motifs usually result in one-dimensional channels[30] instead of

[1]Collaborative Innovation Center of Advanced Nuclear Energy Technology, Institute of Nuclear and New Energy Technology, Tsinghua University, Beijing 100084, China. e-mail: dingxj@mail.tsinghua.edu.cn; yegang@mail.tsinghua.edu.cn

hierarchical cavities[31], exhibiting poor adaptability to accommodate specific guest molecules[32,33]. The stacking manner of the building blocks defines the topology and porosity of HOFs[34–38]. Nevertheless, the weak nature of hydrogen bonds provides the possibility for the hybrid synthesis of hydrogen-bonded networks[39,40]. As a consequence, the employment of polyhedral clusters[41,42], diverse auxiliary interactions[43–45] such as charge-assisted hydrogen bonds[46–49] and multiple components[50–53] expands the opportunity to construct hydrogen-bonded networks based on more advanced, robust building units. At this point, $NH_4^+$, with a tetrahedral geometric structure stabilized by four equivalent N-H bonds and appropriate size ($r_{ionic} \approx 1.5$ Å), behaves in some ways like metal cations in crystal engineering. Cationic interaction of $NH_4^+$ could reliably contribute to electrostatic interactions through charge-assisted hydrogen bonds and potentially regulate the assembly of hydrogen-bonded networks. By donating ionic regulator in the assembly with organic building molecules, we envision that $NH_4^+$ offers tremendous opportunities for constructing advanced supramolecular architectures[54].

In this work, $NH_4^+$ node-assembled polynuclear clusters, akin to the SBUs in reticular chemistry, are exploited in HOF construction for the first time, enabling the formation of a body-centered cubic HOF (TCA_$NH_4$) with distinctive molecular encapsulation, reversible and broadband photochromism, especially sensitive under 400 nm light irradiation. The polynuclear clusters $(NH_4)_4(COOH)_8(H_2O)_2$, denoted as SSBU-$NH_4$−1, sustained by charge-assisted hydrogen bonds, are not as rigid and directional as the classic SBUs stabilized by metal-ligand coordination bonds, which are thus named as supramolecular secondary building units (SSBUs). The unit cell of TCA_$NH_4$ contained an enclosed octahedral cage that could accommodate four haloforms such as $CHCl_3$, $CHBr_3$, and $CHI_3$. All of the encapsulated haloforms exhibited truncated octahedron configurations that suitably matched the enclosed octahedral cage. The distance of adjacent halogens within the encapsulated cavity decreased from Cl-Cl (4.513 Å), Br-Br (4.894 Å) to I-I (3.991 Å) along with decayed fluorescence intensity and shortened lifetime for the corresponding HOFs. Specifically, the host HOF with $CHI_3$ encapsulated in the confined octahedral cages, i.e., TCA_$NH_4$@$CHI_3$, showed fast photochromism (60 s) accompanied by fluorescence quenching outcome. Single crystal−single crystal transformation (SCSCT) analysis and electron paramagnetic resonance (EPR) revealed that $CHI_3$ was photolyzed to metastable $I_2$. More interestingly, such a photochromic reaction, occurring within the isolated octahedral cage of the host HOF, was reversible, and the color of TCA_$NH_4$@$CHI_3$ could be recovered through the heating-induced regeneration of $CHI_3$ from the metastable $I_2$.

## Results

Cubic single crystal of TCA_$NH_4$ was obtained by evaporating the mixed solution of $C_3$-symmetric 4,4′,4″-nitrilotribenzoic acid ($H_3$TCA)[55,56] and $NH_3{\cdot}H_2O$ at room temperature (Supplementary Fig. 1). Blocky TCA_$NH_4$ was also formed by $CH_2Cl_2$ diffusion in the mixed solution of $H_3$TCA and $NH_4Cl$ for weeks (Supplementary Fig. 2). SCXRD results showed $H_3$TCA crystallized in a body-centered cubic system and *I23* space group (Fig. 1a, Supplementary Table 1) with a cell length of 20.9737 Å. $NH_4^+$ served as nodes and bridged two neighboring $H_3$TCA molecules through neutral (2.509 Å) and charge-assisted N-H (+)…O (-) (1.830 Å) hydrogen bonds (Fig. 1b, Supplementary Table 2). Water molecules strengthened the polynuclear clusters through O-H…O (2.069 Å) and N-H…O (2.478 Å) hydrogen bonds. Topologically, $H_3$TCA molecules can be considered as 3-connected nodes, one TCA connected three $NH_4^+$ through O-H…N hrdrogen bonds. Meanwhile, four $NH_4^+$ exactly arranged around two $H_2O$ molecule and connected eight $H_3$TCA molecules within the adjacent unit cell. Consequently, an octahedral cage with a size of about 12 Å was encompassed by $NH_4^+$ and $H_3$TCA molecules (Fig. 1c, Supplementary Fig. 3) and every unit cell contained an isolated cage (Fig. 1b, Supplementary Fig. 4). As expected, $NH_4^+$ acted as the node and every four of them formed supramolecular clusters to connect neighboring cells (Fig. 1d, Supplementary Fig. 5).

Specifically, the above-obtained supramolecular polynuclear clusters $(NH_4)_4(COOH)_8(H_2O)_2$, with well-defined composition and structure sustained by hybrid hydrogen bonds, served as SSBUs in building the cubic network of TCA_$NH_4$ with octahedral cavities. As shown in Supplementary Fig. 5, every $NH_4^+$ bridged two carboxy groups, and two $H_2O$ molecules further linked carboxy groups and $NH_4^+$ from two sides of the SSBUs. The SSBU-$NH_4$-1 could be further considered as two oxygen (two $H_2O$) and four nitrogen (four $NH_4^+$) models. The simplified SSBU-$NH_4$-1 interlaced orthogonally and connected with each other by O-H…O hydrogen bonds (Supplementary Figs. 5, 6). On the whole, the $NH_4^+$ node-assembled clusters not only connected each cell through six surfaces of cubic but also derived into SSBUs to construct advanced frameworks with enclosed octahedral cages.

The enclosed cage or cavity[57] appeared scarce since most HOFs possessed open channels[58–60] and pores[61–63] to transport guest molecules[64–69]. The pore structure of TCA_$NH_4$ appeared an octahedral shape with solvent accessible volume of 14.9 %. However, the synthesized octahedral cavity of TCA_$NH_4$ was isolated and surrounded by crystal water molecules, $NH_4^+$, and TCA molecules. $CO_2$ adsorption isotherm at 273 K of TCA_$NH_4$ was conducted (Supplementary Fig. 7) and the low adsorption capacity indicated the pore can not be accessed by gas molecules at present. Interestingly, we found the void of TCA_$NH_4$ could accommodate homogeneous haloforms including $CHCl_3$, $CHBr_3$, and $CHI_3$. The encapsulation was carried out in solvothermal synthesis at 70 °C in the presence of corresponding trihalomethane molecules. Cubic single crystals of TCA_$NH_4$@$CHCl_3$, TCA_$NH_4$@$CHBr_3$, and TCA_$NH_4$@$CHI_3$ were obtained within about 6 h (Supplementary Fig. 1). The encapsulation could also be achieved by $CH_2Cl_2$ diffusion in mixed solutions of $H_3$TCA and $NH_4Cl$ for weeks. As shown in Fig. 2a, SCXRD results found four homogeneous $CHX_3$ (X = Cl, Br, I) were assembled in the octahedral void within the unit cell. Trihalomethane formed C-H…N hydrogen bonds with four non-adjacent $H_3$TCA molecules (Fig. 2b). The angle of the three hydrogen bonds was all 180° but the distances slightly elongated with the increase of halogen radius (Supplementary Table 3). It was found that four trihalomethanes were precisely accommodated through truncated octahedron configuration (Fig. 2a, Supplementary Fig. 8), and each trihalomethane was parallel to one plane that contained one $H_3$TCA molecule. Additionally, $CHI_3$ formed C-H…I hydrogen bonds (2.817 Å) to enhance the encapsulation (Fig. 2c, Supplementary Table 4). SCXRD results of encapsulated crystals indicated that the encapsulation of trihalomethanes didn't change the crystal structure and the lattice constant and the volume of the unit cell was almost kept constant (Supplementary Table 5). But due to the inefficient and incompact encapsulation of $CHX_3$, the diffracted intensity of halogen atoms especially for iodine was slightly disordered, which implied that the octahedral cages were partly unoccupied by $CHX_3$ molecules. Still, the encapsulation of four trihalomethanes with truncated octahedron shape compatibly matched the octahedral cavity of the hydrogen-bonded framework. Powder X-ray diffraction (PXRD) analysis proved that after encapsulation of trihalomethane, the crystal structure of TCA_$NH_4$ remained stable (Supplementary Fig. 9). Thermogravimetric (TG) results suggested that TCA_$NH_4$, TCA_$NH_4$@$CHCl_3$, TCA_$NH_4$@$CHBr_3$, and TCA_$NH_4$@$CHI_3$ had similar thermal degradation behaviors (Supplementary Fig. 10) due to the encapsulation efficiency were too low and the weight percent of $CHX_3$ were also too low (<40 mg for encapsulation). It can be found that TCA_$NH_4$ held moderate stability after immersing in organic solvent and water (Supplementary Fig. 11) compared with simulated PXRD result. The thermal and solvent stability of crystals indicated that SSBUs built by charged-assisted[70] supramolecular clusters stabilized TCA_$NH_4$ and avoided

https://doi.org/10.1038/s41467-024-47058-1

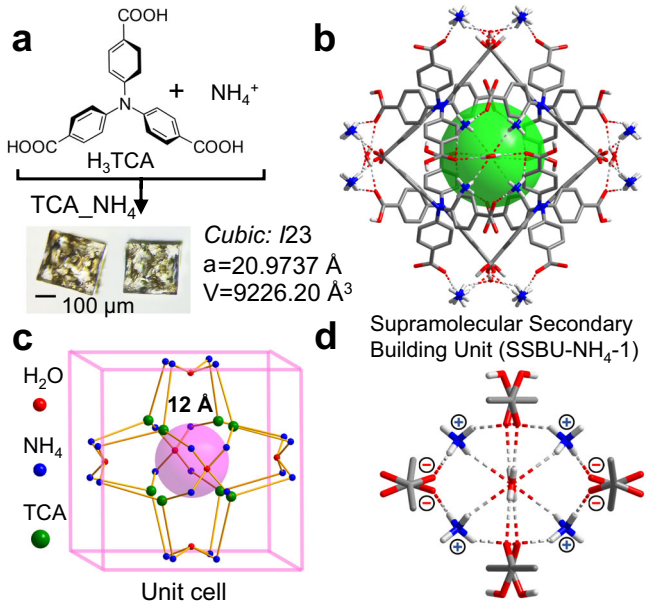


**Fig. 1 | Single-crystal structures of TCA_NH$_4$.** **a** Synthesis and shape of TCA_NH$_4$. **b** NH$_4$ charge-assisted hydrogen-bonded networks and isolated cavity (green color) within the unit cell. **c** Simplified topological network of TCA_NH$_4$ with TCA as a 3-connected nodes and octahedral cage (pink color). **d** SSBU-NH$_4$–1 of $(NH_4)_4(COOH)_8(H_2O)_2$ with concentrated polynuclear clusters and charge-assisted hydrogen bonds. Nonhydrogen bonding hydrogen atoms are omitted for clarity.

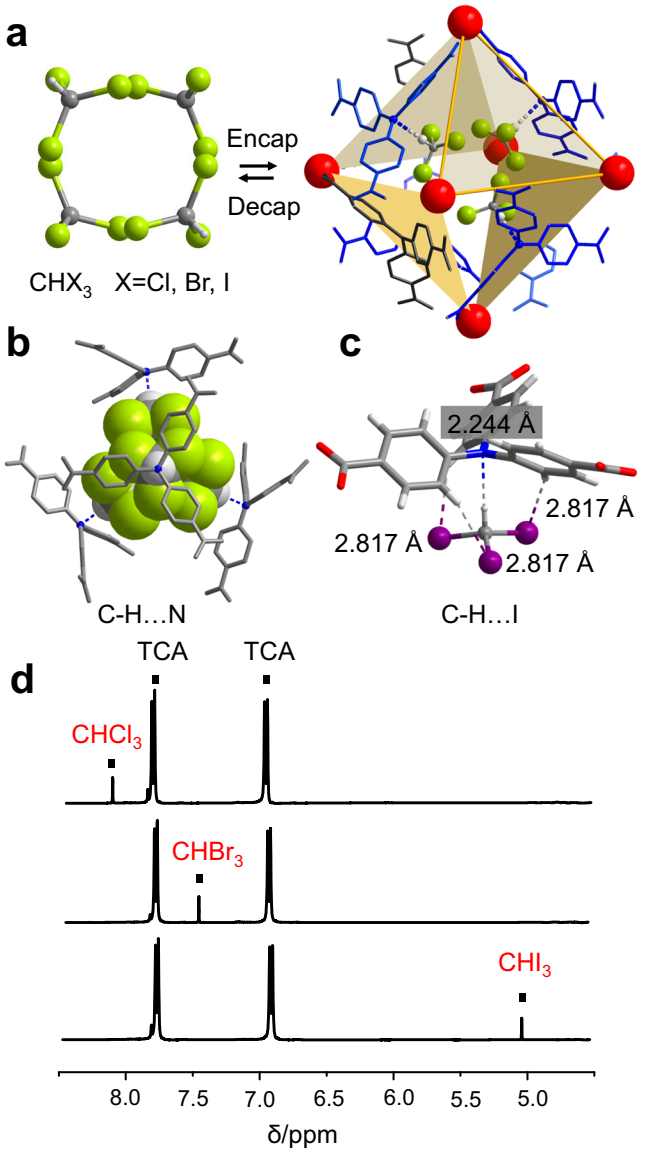


**Fig. 2 | Encapsulation and analysis of haloforms.** **a** Encapsulation and decapsulation of trihalomethane ($CHX_3$, X = Cl, Br, I) within octahedral cage. **b** C-H…N hydrogen bonds between trihalomethane and four noncontiguous TCA. **c** C-H…I hydrogen bonds for encapsulated $CHI_3$. **d** NMR spectra of TCA_NH$_4$@$CHCl_3$, TCA_NH$_4$@$CHBr_3$, and TCA_NH$_4$@$CHI_3$ in DMSO-d6. Nonhydrogen bonding hydrogen atoms are omitted for clarity.

further phase change[71] and collapse of the framework. Taking advantage of the solution-processible benefit of HOFs[72], the encapsulated trihalomethane could be decapsulated by mild hydrolysis of hydrogen-bonded networks. After heating and dissolving in dimethyl sulfoxide (DMSO), nuclear magnetic resonance (NMR) results revealed that the encapsulated TCA_NH$_4$@$CHCl_3$, TCA_NH$_4$@$CHBr_3$, and TCA_NH$_4$@$CHI_3$ were observed to decompose and trihalomethane were observed to release (Fig. 2d). The encapsulation efficiency was roughly estimated by intensity of NMR spectra and all encapsulated samples were <10%, showing an incompact capture of trihalomethane.

With a closer examination, although the trihalomethane molecules were all encapsulated in truncated octahedrons, their configuration appeared slightly different. As shown in Fig. 3a, the distances of the nearest halogen atoms were classified as X1-X1, X1-X2, and X1-X3 (X = Cl, Br, I, Supplementary Fig. 12). Each classification included two directions. SCXRD results revealed that the distances of X1-X1 and X1-X2 were almost maintained after assembling $CHX_3$ (Fig. 3b). However, the distance of X1-X3 decreased from Cl1-Cl3 (4.513 Å) to Br1-Br3(4.894 Å), and then to I1-I3(3.99 Å). The shortened distances of adjacent halogen atoms provided the possibility for bonding reactions, especially for iodine. The color of TCA_NH$_4$ was changed after encapsulating haloforms, particularly for TCA_NH$_4$@$CHBr_3$ and TCA_NH$_4$@$CHI_3$. The color of crystals was resulted from the guest trihalomethane. In addition, the fluorescence emission spectrum of TCA_NH$_4$ showed no shift after assembling with $CHCl_3$ and $CHBr_3$ (Fig. 4a), but the emission spectrum red-shifted from 430 nm to 480 nm for TCA_NH$_4$@$CHI_3$ attributed to the absorbed energy transfer from $H_3TCA$ to $CHI_3$. The absorbed energy transfer from $H_3TCA$ to $CHX_3$ resulted red-shift of emission spectrum are largely determined by two reasons, one is the distances between $H_3TCA$ and $CHX_3$, the other is the heavy atom effect-induced fluorescence quenching. The distances from $H_3TCA$ to $CHCl_3$ and $CHBr_3$ are 2.805 Å and 3.007 Å, respectively (Supplementary Table 3), which are longer than the distance from $H_3TCA$ to $CHI_3$ (2.244 Å). Therefore, the closer distance and heavy atom effect contributed to the absorbed energy transfer from $H_3TCA$ to $CHI_3$ while the longer distances prevented the absorbed energy transfer from $H_3TCA$ to $CHCl_3$ and $CHBr_3$. Solid-state fluorescence reflection spectrum indicated that the fluorescence efficiency of TCA_NH$_4$ decreased (Supplementary Fig. 13) after encapsulating trihalomethane, because of heavy atom effect-induced fluorescence quenching. In the same way, the excitation spectrum of TCA_NH$_4$ also decreased after assembling haloforms, and the maximum excitation wavelength slightly blue-shifted from TCA_NH$_4$ at 410 nm to TCA_NH$_4$@$CHI_3$ at 380 nm (Supplementary Fig. 14) because of higher excitation energy for hydrogen-bonded networks of $H_3TCA$ and trihalomethane. The lifetime of TCA_NH$_4$ was 2.09 ns (Fig. 4b, Supplementary Table 6) and it slightly decreased to 2.05 ns and 1.69 ns after assembling $CHCl_3$ and $CHBr_3$, respectively, following the quenching mechanism. But the lifetime increased to 2.43 ns after assembling $CHI_3$ maybe due to the energy exchange between excited species of $H_3TCA$ and $CHI_3$ contributing to the delayed decay of the excited state. Solid-state absorption spectrum proved the structure of TCA_NH$_4$ did not vary obviously when compared with TCA_NH$_4$@$CHCl_3$,

https://doi.org/10.1038/s41467-024-47058-1

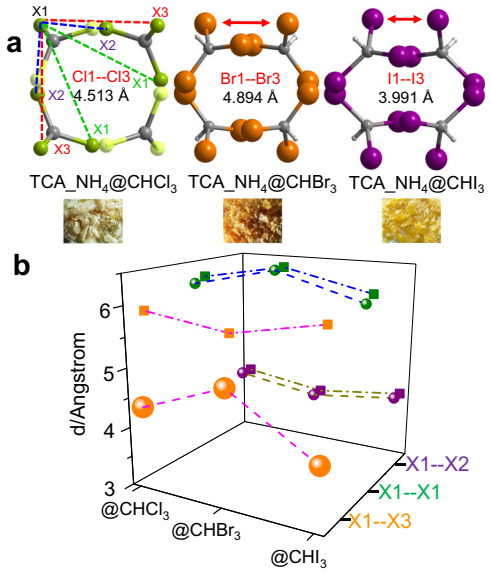


**Fig. 3 | Configuration of encapsulated haloforms. a** Color and configuration of encapsulated trihalomethane with defined distances between X1 and its neighboring atoms, the horizontal X1-X3 were decreased. **b** Distances of neighboring halogen atoms in encapsulated TCA_NH$_4$.

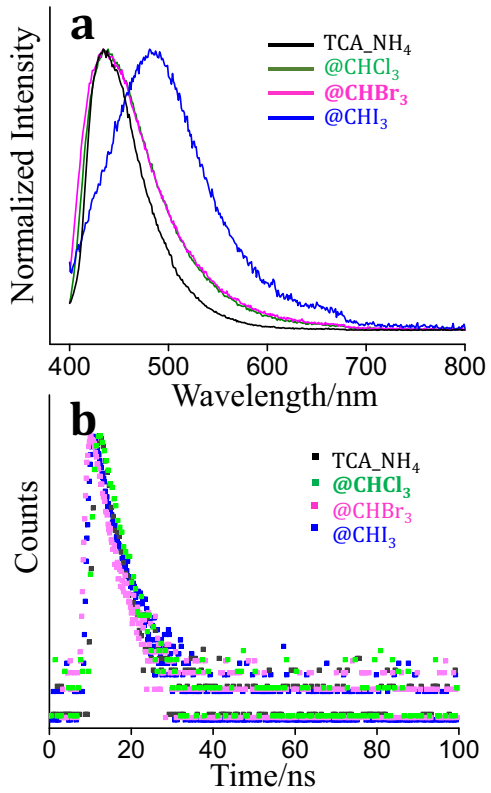


**Fig. 4 | Spectroscopic analysis of encapsulated haloforms. a** Normalized emission spectrum of TCA_NH$_4$, TCA_NH$_4$@CHCl$_3$, TCA_NH$_4$@CHBr$_3$, and TCA_NH$_4$@CHI$_3$ excited at 360 nm. **b** Decay profile of TCA_NH$_4$, TCA_NH$_4$@CHCl$_3$, TCA_NH$_4$@CHBr$_3$, and TCA_NH$_4$@CHI$_3$.

TCA_NH$_4$@CHBr$_3$, and TCA_NH$_4$@CHI$_3$ (Supplementary Fig. 15). The absorption peak appeared at 400 nm, indicating the crystals were more sensitive to ultraviolet light, especially for 400 nm of light. The above results indicated that the octahedral cavity within TCA_NH$_4$ precisely accommodated four trihalomethanes with matched truncated octahedron shape. The color of assembled crystals changed by varied guest molecules. The fluorescence efficiency decreased after encapsulating haloforms. Particularly, the distances between adjacent halogen atoms were shortened especially for TCA_NH$_4$@CHI$_3$, which promoted energy transfer from excited H$_3$TCA to CHI$_3$ and prolonged lifetime and provided the possibility for bonding formation.

The encapsulation of photoactive CHI$_3$ inspired us to examine the photo-responsive behaviors of TCA_NH$_4$@CHI$_3$. Interestingly, TCA_NH$_4$@CHI$_3$ showed a 60-s fast photochromic phenomenon under irradiation of a UV-vis xenon lamp at 400 nm with a light power density of about 200 mW/cm$^2$ (Fig. 5a). SCSCT analysis revealed the distance of I1-I3 was further shortened to 2.822 Å of metastable I$_2$ approximately equivalent to I$_2$ (2.6 Å), and yellow TCA_NH$_4$@CHI$_3$ quickly transformed to brown TCA_NH$_4$@I$_2$. The solid-state absorption spectrum recorded the formation of metastable I$_2$ (Fig. 5b). The absorption peak of CHI$_3$ at 418 nm decreased and the absorption peak of metastable I$_2$ at 450 nm appeared after irradiation with UV-vis light for 5 min. Electron paramagnetic resonance (EPR) of TCA_NH$_4$@CHI$_3$ was conducted to examine the photolysis of iodoform. Disordered signals of TCA_NH$_4$@CHI$_3$ turned to specific radical signals (Fig. 5c) after in-situ illumination by a UV-vis light source with a light power density of about 200 mW/cm$^2$. The $g$ value at about 2.005 indicated the free electron resulted from the homolytic cleavage of the C-I bond[73] (Supplementary Fig. 16). Accordingly, TCA_NH$_4$@CHCl$_3$ and TCA_NH$_4$@CHBr$_3$ were also irradiated by a UV-vis light source to examine free radical signals. As shown in Supplementary Figs. 17 and 18, disordered signals indicated that no free radicals were generated or chemical bonds broken after irradiation. The absence of free radicals for TCA_NH$_4$@CHCl$_3$ and TCA_NH$_4$@CHBr$_3$ under illumination might be explained by two reasons. First, CHBr$_3$ and CHCl$_3$ are not intrinsically photosensitive. Meanwhile, the distances of Cl-Cl (4.513 Å) and Br-Br (4.894 Å) are longer than that of I-I (3.991 Å). As a result, only encapsulated photosensitive CHI$_3$ with a short distance of I-I bond showed unique reversible photo/thermal transformation. The SCXRD and EPR results proved that the photochromic reaction of TCA_NH$_4$@CHI$_3$ stemmed from photolysis of iodoform and the formation of metastable I$_2$. We consider the free radical generated within the enclosed cavity could further react with metastable I$_2$, on account of the isolated octahedral cavity providing a spatially-confined platform as nanoreactor that could stabilize free radicals and metastable I$_2$. As a result, after the photochromic reaction, brown TCA_NH$_4$@I$_2$ was immediately immersed in liquid paraffin to equably heat under a dark environment for an hour. As expected, the brown crystal returned to yellow and solid-state absorption spectrum results confirmed the recovery of iodoform (Fig. 5a, d). To examine the stability of the crystal after photo/thermal transformation, PXRD of TCA_NH$_4$@CHI$_3$ before and after irradiation under Xe lamp, as well as after thermal recovery, were conducted. As shown in Supplementary Fig. 19, the crystal structures maintained intact after reversible photo/thermal transformation as compared with the simulated PXRD pattern. The results indicated that HOFs encapsulated with CHI$_3$ could afford a stable photochromic material. Photochromic reaction and thermal recovery were repeated to investigate the reversible cycle of photo-responsive performance of TCA_NH$_4$@CHI$_3$. After repeating 5 rounds of irradiating and heating processes, TCA_NH$_4$@CHI$_3$ still maintained photochromic activity and the yellow crystal was still renewed (Supplementary Figs. 20, 21). The above results further proved that fast photochromic reaction and thermal recovery of encapsulated CHI$_3$ within an octahedral cage maintained a steady process to contribute as a new type of photochromic material.

For a photochromic process, usually, the dependence of light wavelength with a limited range restricts general applications in environment probing[74–76]. HOFs have shown great potential in luminescent fields[77]. Surprisingly, TCA_NH$_4$@CHI$_3$ not only turned color at 400 nm of light but also held a broad photosensitive scope ranging

https://doi.org/10.1038/s41467-024-47058-1

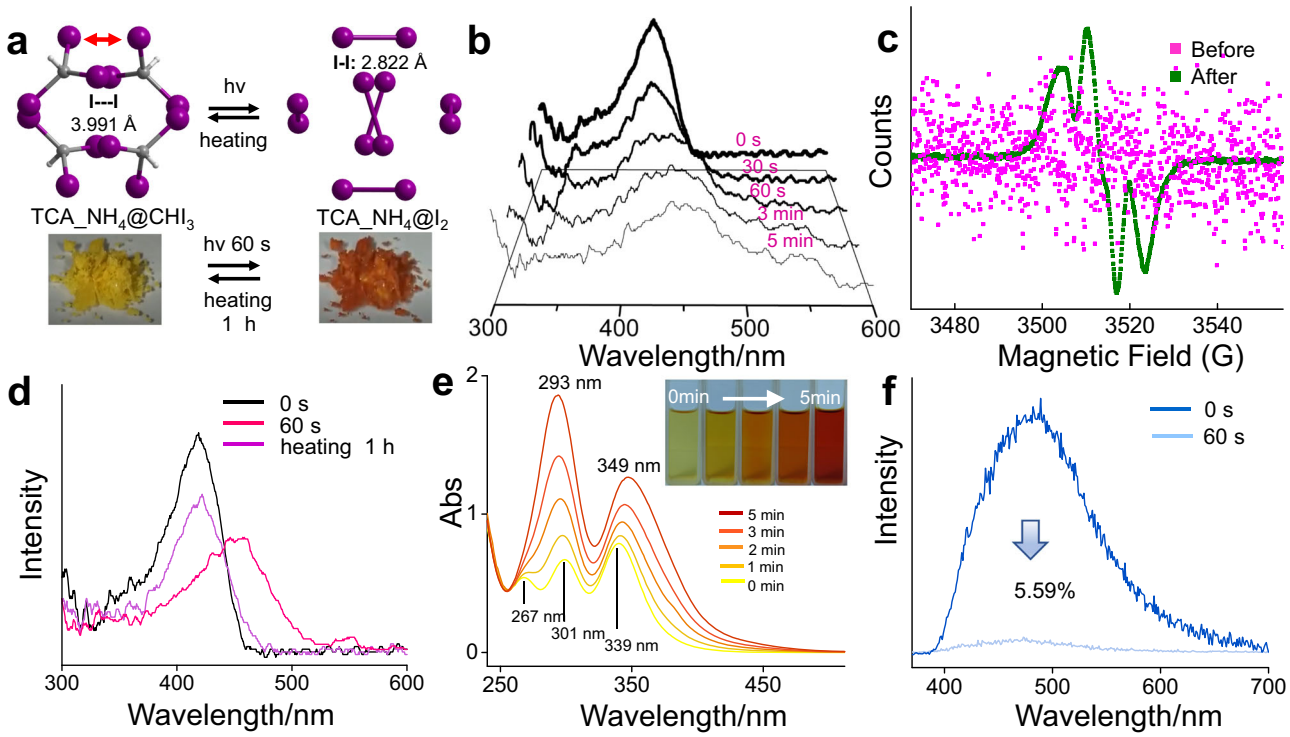


**Fig. 5 | Reversible photo/thermal transformation and characterization of encapsulated $CHI_3$.** **a** Photochromic reaction and thermal recovery of TCA_$NH_4$@$CHI_3$. **b** Solid-state absorption spectrum of TCA_$NH_4$@$CHI_3$ irradiated with a Xe lamp (400 nm, 200 mW/cm$^2$). **c** EPR spectrum of TCA_$NH_4$@$CHI_3$ before and after irradiation under a UV-vis light source (200 mW/cm$^2$). **d** Solid-state absorption spectrum of TCA_$NH_4$@$CHI_3$ after heating for an hour under dark environment. **e** UV-vis absorption spectrum of solid $CHI_3$ dissolved in ethanol (6 g/L) under irradiation with a Xe lamp for 5 min. **f** In-situ emission spectrum of TCA_$NH_4$@$CHI_3$ before and after irradiation with a Xe lamp for 60 s.

from X-ray, ultraviolet light, sunlight, and even low-energy light-emitting diode (8 mW/cm$^2$). The varied light source and light intensity made TCA_$NH_4$@$CHI_3$ with different photosensitive efficiency ranging from 60 s to 5 min (Supplementary Table 7). The broad photosensitive scope and fast photochromic efficiency of TCA_$NH_4$@$CHI_3$ originated from the combination of multiple effects. Firstly, as shown by SCXRD in Fig. 3b, the shortened distance between adjacent I1-I3 in the enclosed octahedral cavity provided the possibility for a bond-formation reaction. Secondly, the decreased fluorescence efficiency of TCA_$NH_4$ after assembling trihalomethane promoted the transfer of the absorbed energy from $H_3$TCA to $CHI_3$, so that $CHI_3$ was energetic for potential physicochemical reactions. Thirdly, $CHI_3$ is intrinsically photosensitive. As shown in Fig. 5e, the pure $CHI_3$ powder was dissolved in ethanol (6 g/L) and irradiated under a xenon lamp with a light power density of about 200 mW/cm$^2$. The color of $CHI_3$ quickly turned brown within minutes (Inserted graph) and the UV-vis absorption spectrum proved the generation of $I_2$. The characteristic peaks of $CHI_3$ at 267 nm, 301 nm, and 339 nm decreased and characteristic peaks of $I_2$ at 293 nm and 349 nm appeared. Solid powder of $CHI_3$ also showed photosensitive reaction except that the color of the powder showed no visible change under 10 min irradiation with Xe lamp (Supplementary Fig. 22). Nevertheless, after irradiation with Xe lamp, both dissolved $CHI_3$ and solid powder of $CHI_3$ could not recover whether heating or standing due to the lack of an enclosed void for the restriction and stabilization of metastable products and free radicals. In addition, the fluorescence emission spectrum of TCA_$NH_4$@$CHI_3$ was markedly quenched to 5.59% after in-situ irradiation with Xe lamp for 60 s because of fluorescence quenching caused by metastable $I_2$ (Fig. 5f), and emission spectrum blue-shifted from 480 nm to 450 nm (Supplementary Fig. 23) that was close to TCA_$NH_4$@$CHCl_3$ and TCA_$NH_4$@$CHBr_3$ due to the break of energy transfer between $H_3$TCA and $CHI_3$. The excitation spectrum was also quenched after the photochromic reaction (Supplementary Fig. 24) and the lifetime slightly decreased (Table S6, 2.43 ns vs 2.37 ns). The above results confirmed that the octahedral cavity within TCA_$NH_4$ offered unique nanoreactors for photochromic reaction and spatially-confined thermal recovery of $CHI_3$. The fast photochromic efficiency, broad photosensitivity, and unique fluorescence quenching of TCA_$NH_4$@$CHI_3$ showed great potential in sensing and environmental probing.

## Discussion

In summary, taking advantage of $NH_4^+$ as nodes to bridge $H_3$TCA building blocks through charge-assisted hydrogen bonds, supramolecular polynuclear clusters $(NH_4)_4(COOH)_8(H_2O)_2$ were obtained and appropriately served as SSBU-$NH_4$-1 to construct a distinctive body-centered cubic hydrogen-bonded organic framework. The assembled TCA_$NH_4$ contained enclosed octahedral cages that precisely accommodated four homogenous trihalomethanes including $CHCl_3$, $CHBr_3$, and $CHI_3$. The truncated octahedron form of encapsulated trihalomethane compatibly matched the octahedral cavity of TCA_$NH_4$ through strong C-H…N hydrogen bonds. Besides, the fluorescence emission efficiency of TCA_$NH_4$ decreased after assembling different haloforms, promoting the transfer of the absorbed light energy to haloforms. The distances between adjacent halogen atoms within the octahedral cavity were shortened especially for $CHI_3$. As a result, TCA_$NH_4$@$CHI_3$ showed fast photochromic efficiency, broad photosensitivity, and unique fluorescence quenching behavior. The brown TCA_$NH_4$@$I_2$ could be recovered to TCA_$NH_4$@$CHI_3$ after heating due to the enclosed octahedral cages that provided spatially-confined nanoreactors to stabilize the free radical and metastable products. This study provides creative insights into the framework chemistry of HOFs and particularly an adaptable strategy for HOF construction from supramolecular polynuclear clusters sustained by charge-assisted H-bonds. The established methodology would expand the

framework topology of HOFs and accelerate the customized development of HOFs with predetermined architectures. Moreover, this study also provided a promising prototype of sensitive photochromic materials based on $CHI_3$ encapsulation within the isolated cavities of HOF nanoreactor platforms.

## Methods

### General remark

4,4′,4″-nitrilotribenzoic acid ($H_3TCA$) and other reagents were purchased from Sinopharm Chemical Reagent Co., Ltd. in analytical grade. Powder X-ray diffraction data (PXRD) were performed by a Rigaku MiniFlex600 (40 kV, 15 mA) with a graphite-monochromatized Cu Kα radiation. Electron paramagnetic resonance (EPR) was conducted on a spectrometer (JEOL, JES FA-200). The data was collected with microwave field power of 0.7 mW. The modulation frequency was 100 kGHz and the microwave frequency was 9.7 GHz. Thermogravimetric analysis (TGA) was conducted on an SDT Q600 analyzer with a heating rate of 10 °C/min under $N_2$ (100 mL/min) atmosphere. $^1$H NMR spectra was conducted in DMSO-d6 solution by JNM-ECZ400S (400 MHz) spectrometer.

### Synthesis of single crystals

**TCA_NH$_4$.** 120 mg $H_3TCA$ was dissolved in 0.8 mL N, N-Dimethylformamide (DMF) in a vial. 20 μL $NH_3H_2O$ was added and the mixed solution was slightly heated to get a clear solution. Then the solution was stood for evaporation and a cubic single crystal can be obtained after 3 weeks (Supplementary Fig. 1). Block single crystals also can be obtained by $CH_2Cl_2$ diffusion in a mixed solution of $H_3TCA$ and $NH_4Cl$ for 3 weeks.

**TCA_NH$_4$@CHCl$_3$.** 120 mg $H_3TCA$ was dissolved in 1 mL DMF in a vial. 40 μL $NH_3H_2O$ was added to get precipitation. 30 μL deionized water was added and the vial was slightly heated to get a clear solution. 30 μL $CHCl_3$ was added and the mixed solution was quietly evaporated at 70 °C. Cubic single crystals can be obtained within 6 h (Supplementary Fig. 1).

**TCA_NH$_4$@CHBr$_3$.** 120 mg $H_3TCA$ was dissolved in 0.8 mL DMF in a vial. 30 μL $NH_3H_2O$ was added to get precipitation. 40 μL deionized water was added and the vial was slightly heated to get a clear solution. 30 μL $CHBr_3$ was added and the mixed solution was quietly evaporated at 70 °C. Cubic single crystals can be obtained within 6 h (Supplementary Fig. 1).

**TCA_NH$_4$@CHI$_3$.** 200 mg $H_3TCA$ was dissolved in 0.8 mL DMF in a vial. 40 μL $NH_3H_2O$ was added to get precipitation. 80 μL deionized water was added and the vial was slightly heated to get a clear solution. 20 mg $CHI_3$ was added and the vial was heated to get a clear solution. Then the mixed solution was quietly evaporated at 66 °C under a dark environment. Yellow single crystals can be obtained within 6 h (Supplementary Fig. 1).

The encapsulation of $CHCl_3$, $CHBr_3$, and $CHI_3$ can also be obtained by $CH_2Cl_2$ diffusion in a mixed solution of $H_3TCA$, $NH_4Cl$, and trihalomethane for 3 weeks.

### Single-crystal X-ray diffraction analysis

Single crystal measurement was conducted on a Bruker APEX-II CCD with Cu K$\alpha$ ($\lambda$ = 1.54184 Å) X-ray sources. SADABS-2016/2(Bruker,2016/2) was used for absorption correction. The structure refinement was performed with Olex2 1.5 program. The structure was solved by ShelXT intrinsic phasing method and was refined by ShelXL least-squares techniques. All nonhydrogen atoms were refined with anisotropic displacement parameters. SQUEEZE function from PLATON program was taken to treat disordered solvent molecules in voids for TCA_NH$_4$. The bond length of C-I bond was preset to be 2.0 Å in TCA_NH$_4$@I$_2$ using DFIX command to avoid disordered and free carbon atoms. Data collection and refinement details are listed in Table S1 and supplementary crystallographic CIF files have been deposited on Cambridge Crystallographic Data Centre (CCDC) with the number 2309944 for TCA_NH$_4$, 2309942 for TCA_NH$_4$@CHCl$_3$, 2309941 for TCA_NH$_4$@CHBr$_3$, 2309943 for TCA_NH$_4$@CHI$_3$, and 2309940 for TCA_NH$_4$@I$_2$.

### Solid-state spectroscopy measurement

Solid-state absorption spectroscopy was measured on a CRAIC 20/30 microspectrophotometer. A Xe lamp (90 W) was used as UV-vis and fluorescence source for measurement. For the UV-vis absorption test, parameters were set as Time1 = 57 ms: Objective = 15X: Aperture = 4 × 4 mm$^2$. For the fluorescence reflection test, 365 nm channel was used and parameters were set as Time1 = 1000 ms: Objective = 15X: Aperture = 4 × 4 mm$^2$.

### The fluorescence emission and absorption measurement

The data was collected on a FLS1000 spectrometer with Visible/red-PMT detector and Xe lamp (300 W) as the light source for measurement. The excitation wavelength was 360 nm (bandwidth: 1 nm) and the emission wavelength was 470 nm (bandwidth: 0.4 nm). A nF920 nanosecond flashlamp ($H_2$ padded in chamber) was used for lifetime measurement. The time range was <500 millisecond and channels were fixed to 1024, and stop condition was set to 1000 counts. The decay lifetime was fitted according to multiexponential function models. The matching rate of fitting results were estimated by $\chi^2$ (1.0-1.1, Table S6).

### Photochromic reaction and thermal recovery

The synthesized yellow TCA_NH$_4$@CHI$_3$ crystal was washed with dimethyl formamide (DMF) and acetone and then dried out. The yellow crystal was put into a vial and heated at 60 °C under a dark environment for 30 min to activate the crystal. Then the crystal was put under a Xe lamp (200 mW/cm$^2$, 400 nm) to be exposed for 1 min or directly exposed under intense sunlight for 1–5 min. The color of the crystal quickly turned to brown and then the crystal was immediately immersed in liquid paraffin to equably heat at 100 °C for an hour under dark surroundings. The color of the crystal recovered to yellow. The crystal was taken out and washed with organic solvent to remove liquid paraffin and then dried out. The recovered crystal was preserved under dark surroundings.

## Data availability

The data that support the findings of this study are available in the Supplementary Information. The X-ray crystallographic files for structures in this study have been deposited at the Cambridge Crystallographic Data Centre (CCDC), with numbers 2309940-2309944. These data can be obtained free of charge from The Cambridge Crystallographic Data Centre via www.ccdc.cam.ac.uk/getstructures. The source data generated in this study have been deposited in the Figshare database under accession code DOI: 10.6084/m9.figshare.25272415. Source data are provided with this paper.

## References

1. Katsoulidis, A. P. et al. Chemical control of structure and guest uptake by a conformationally mobile porous material. *Nature* **565**, 213–217 (2019).
2. Liu Y. & Zhao, W. Chloride capture using a C-H hydrogen-bonding cage. *Science* **365**, 159–161 (2019).
3. Han, B. et al. Postsynthetic metalation of a robust hydrogen-bonded organic framework for heterogeneous catalysis. *J. Am. Chem. Soc.* **141**, 8737–8740 (2019).

4. Gong, W. et al. Permanent porous hydrogen-bonded frameworks with two types of bronsted acid sites for heterogeneous asymmetric catalysis. *Nat. Commun.* **10**, 600 (2019).
5. Deng, J.-H. π-π stacking interactions: non-negligible forces for stabilizing porous supramolecular frameworks. *Sci. Adv.* **6**, eaax9976 (2020).
6. Yang, Y. et al. Ethylene/ethane separation in a stable hydrogen-bonded organic framework through a gating mechanism. *Nat. Chem.* **13**, 933–939 (2021).
7. Cai, Y. et al. Pore modulation of hydrogen-bonded organic frameworks for efficient separation of propylene. *Angew. Chem. Int. Ed.* **62**, e202308579 (2023).
8. Liu, Y. et al. Hydrogen-bonded metal-nucleobase frameworks for efficient separation of xenon and krypton. *Angew. Chem. Int. Ed.* **61**, e202117609 (2022).
9. Zeng, H. et al. Orthogonal-array dynamic molecular sieving of propylene/propane mixtures. *Nature* **595**, 542–548 (2021).
10. Samanta, J. et al. An ultra-dynamic anion-cluster-based organic framework. *Chem* **8**, 253–267 (2022).
11. Liu, Y., Hu, C., Comotti, A. & Ward, M. D. Supramolecular archimedean cages assembled with 72 hydrogen bonds. *Science* **333**, 436–440 (2011).
12. Zhu, Q. et al. Analogy powered by prediction and structural invariants: computationally led discovery of a mesoporous hydrogen-bonded organic cage crystal. *J. Am. Chem. Soc.* **144**, 9893–9901 (2022).
13. He, Y. et al. Hierarchical self-assembly of DNA into symmetric supramolecular polyhedra. *Nature* **452**, 198–201 (2008).
14. Liang, W. et al. Enzyme encapsulation in a porous hydrogen-bonded organic framework. *J. Am. Chem. Soc.* **141**, 14298–14305 (2019).
15. Chen, G., Huang, S., Ma, X., He, R. & Ouyang, G. Encapsulating and stabilizing enzymes using hydrogen-bonded organic frameworks. *Nat. Protoc.* **18**, 2032–2050 (2023).
16. Hisaki, I. et al. Acid responsive hydrogen-bonded organic frameworks. *J. Am. Chem. Soc.* **141**, 2111–2121 (2019).
17. Farid, N. et al. Supermolecular building blocks (SBBs) for the design and synthesis of highly porous metal-organic frameworks. *J. Am. Chem. Soc.* **130**, 1833–1835 (2008).
18. Yang, S. Supramolecular lattices from tetrahedral nanobuilding blocks. *Science* **348**, 396–397 (2015).
19. Zhang, Z., Ye, Y., Xiang, S. & Chen, B. Exploring multifunctional hydrogen-bonded organic framework materials. *Acc. Chem. Res.* **55**, 3752–3766 (2022).
20. Ermer, O. Fivefold-diamond structure of adamantane–1,3,5,7-tetracarboxylic acid. *J. Am. Chem. Soc.* **110**, 3474–3754 (1988).
21. Malek, N., Maris, T., Simard, M. & Wuest, J. D. Molecular tectonics. selective exchange of cations in porous anionic hydrogen-bonded networks built from derivatives of tetraphenylborate. *J. Am. Chem. Soc.* **127**, 5910–5916 (2005).
22. Soleimani Abhari, P. et al. Recent progress in gas separation platforms based on hydrogen-bonded organic frameworks (HOFs). *Inorg. Chem. Front.* **10**, 6134–6159 (2023).
23. Lin, R.-B. & Chen, B. Hydrogen-bonded organic frameworks: chemistry and functions. *Chem* **8**, 2114–2135 (2022).
24. Song, X. et al. Design rules of hydrogen-bonded organic frameworks with high chemical and thermal stabilities. *J. Am. Chem. Soc.* **144**, 10663–10687 (2022).
25. Lin, Z. J., Mahammed, S. A. R., Liu, T. F. & Cao, R. Multifunctional porous hydrogen-bonded organic frameworks: current status and future perspectives. *ACS Cent. Sci.* **8**, 1589–1608 (2022).
26. Xi, X.-J. et al. Robust porous hydrogen-bonded organic frameworks: synthesis and applications in gas adsorption and separation. *Giant* **16**, 100181 (2023).
27. Tohnai, N. et al. Well-designed supramolecular clusters comprising triphenylmethylamine and various sulfonic acids. *Angew. Chem. Int. Ed.* **46**, 2220–2223 (2007).
28. Oka, K. et al. Ice-like dynamics of water clusters. *J. Phys. Chem. Lett.* **15**, 267–271 (2024).
29. Qin, W. K. et al. Reticular synthesis of hydrogen-bonded organic frameworks and their derivatives via mechanochemistry. *Angew. Chem. Int. Ed.* **61**, e202202089 (2022).
30. Chen, X. et al. A proton conductive porous framework of an 18-crown-6-ether derivative networked by rigid hydrogen bonding modules. *Angew. Chem. Int. Ed.* **61**, e202211686 (2022).
31. Shields, C. E. et al. Experimental confirmation of a predicted porous hydrogen-bonded organic framework. *Angew. Chem. Int. Ed.* **62**, e202303167 (2023).
32. Pulido, A. et al. Functional materials discovery using energy-structure-function maps. *Nature* **543**, 657–664 (2017).
33. Cui, P. et al. An expandable hydrogen-bonded organic framework characterized by three-dimensional electron diffraction. *J. Am. Chem. Soc.* **142**, 12743–12750 (2020).
34. Liu, Y. et al. Hybrid hydrogen-bonded organic frameworks: structures and functional applications. *Chem. -Eur. J.* **29**, e202202655 (2023).
35. Wang, B., Lin, R. B., Zhang, Z., Xiang, S. & Chen, B. Hydrogen-bonded organic frameworks as a tunable platform for functional materials. *J. Am. Chem. Soc.* **142**, 14399–14416 (2020).
36. Yang, Y. et al. An ultramicroporous hydrogen-bonded organic framework exhibiting high $C_2H_2/CO_2$ separation. *Angew. Chem. Int. Ed.* **61**, e202207579 (2022).
37. Chen, L. et al. A flexible hydrogen-bonded organic framework constructed from a tetrabenzaldehyde with a carbazole N-H binding site for the highly selective recognition and separation of acetone. *Angew. Chem. Int. Ed.* **61**, e202213959 (2022).
38. Li, Y. L. et al. Record complexity in the polycatenation of three porous hydrogen-bonded organic frameworks with stepwise adsorption behaviors. *J. Am. Chem. Soc.* **142**, 7218–7224 (2020).
39. Hashimoto, T., Oketani, R., Nobuoka, M., Seki, S. & Hisaki, I. Single crystalline, non-stoichiometric cocrystals of hydrogen-bonded organic frameworks. *Angew. Chem. Int. Ed.* **62**, e202215836 (2023).
40. Bao, Z. et al. Fine tuning and specific binding sites with a porous hydrogen-bonded metal-complex framework for gas selective separations. *J. Am. Chem. Soc.* **140**, 4596–4603 (2018).
41. Montis, R. et al. Complex structures arising from the self-assembly of a simple organic salt. *Nature* **590**, 275–278 (2021).
42. Halliwell, C. A. et al. Hierarchical assembly of a micro- and macroporous hydrogen-bonded organic framework with tailored single-crystal size. *Angew. Chem. Int. Ed.* **61**, e202208677 (2022).
43. Madueno, R., Raisanen, M. T., Silien, C. & Buck, M. Functionalizing hydrogen-bonded surface networks with self-assembled monolayers. *Nature* **454**, 618–621 (2008).
44. Sun, Y. et al. Bio-inspired synthetic hydrogen-bonded organic frameworks for efficient proton conduction. *Adv. Mater.* **35**, e2208625 (2023).
45. Zhang, A. A. et al. Partial metalation of porphyrin moieties in hydrogen-bonded organic frameworks provides enhanced $CO_2$ photoreduction activity. *Angew. Chem. Int. Ed.* **61**, e202203955 (2022).
46. Bai, X.-T. et al. Ultra-high proton conductivity iHOF based on guanidinium arylphosphonate for proton exchange membrane fuel cells. *Chem. Mater.* **35**, 3172–3180 (2023).
47. Ding, X. et al. Binary solvent regulated architecture of ultramicroporous hydrogen-bonded organic frameworks with tunable polarization for highly-selective gas separation. *Angew. Chem. Int. Ed.* **61**, e202116483 (2022).

48. Zhou, Y. et al. Tuning pore polarization to boost ethane/ethylene separation performance in hydrogen-bonded organic frameworks. *Angew. Chem. Int. Ed.* **62**, e202305041 (2023).
49. Li, Y. et al. Guest exchange through facilitated transport in a seemingly impenetrable hydrogen-bonded framework. *J. Am. Chem. Soc.* **140**, 12915–12921 (2018).
50. Zhang, J., Feng, Y., Staples, R. J., Zhang, J. & Shreeve, J. M. Taming nitroformate through encapsulation with nitrogen-rich hydrogen-bonded organic frameworks. *Nat. Commun.* **12**, 2146 (2021).
51. Ami, T., Oka, K., Tsuchiya, K. & Tohnai, N. Porous organic salts: diversifying void structures and environments. *Angew. Chem. Int. Ed.* **61**, e202202597 (2022).
52. Han, Z. et al. High-efficiency lithium-ion transport in a porous coordination chain-based hydrogen-bonded framework. *J. Am. Chem. Soc.* **145**, 10149–10158 (2023).
53. Xing, G. et al. A double helix of opposite charges to form channels with unique $CO_2$ selectivity and dynamics. *Chem. Sci.* **10**, 730–736 (2019).
54. Ding, X. et al. Charge-assisted hydrogen-bonded organic frameworks with inorganic ammonium regulated switchable open polar sites. *Small* **19**, e2207771 (2023).
55. Nandi, S., Chakraborty, D. & Vaidhyanathan, R. A permanently porous single molecule H-bonded organic framework for selective $CO_2$ capture. *Chem. Commun.* **52**, 7249–7252 (2016).
56. Cai, Y. et al. Robust microporous hydrogen-bonded organic framework for highly selective purification of methane from natural gas. *Micropor. Mesopor. Mater.* **352**, 112495 (2023).
57. Marchetti, D. et al. Selective and reversible solvent uptake in Tetra-4-(4-pyridyl) phenylmethane-based supramolecular organic frameworks. *Chem. -Eur. J.* **28**, e202202977 (2022).
58. Sei, H. et al. Cage-like sodalite-type porous organic salts enabling luminescent molecule's incorporation and room-temperature phosphorescence induction in air. *Small* **19**, e2301887 (2023).
59. Xie, Y., Ding, X., Wang, J. & Ye, G. Hydrogen-bonding assembly meets anion coordination chemistry: framework shaping and polarity tuning for xenon/krypton separation. *Angew. Chem. Int. Ed.* **62**, e202313951 (2023).
60. Sei, H., Oka, K. & Tohnai, N. Incorporation of coronene into cage-like porous organic salts and induction of its room-temperature phosphorescence in air. *ChemNanoMat* **9**, e202300248 (2023).
61. Liu, X. et al. A robust redox-active hydrogen-bonded organic framework for rechargeable batteries. *J. Mater. Chem. A.* **10**, 1808–1814 (2022).
62. Chen, Y. et al. Ultramicroporous hydrogen-bonded organic framework material with a thermoregulatory gating effect for record propylene separation. *J. Am. Chem. Soc.* **144**, 17033–17040 (2022). 37.
63. Chen, S. et al. Photo responsive electron and proton conductivity within a hydrogen-bonded organic framework. *Angew. Chem. Int. Ed.* **62**, e202308418 (2023).
64. Chen, G. et al. Hydrogen-bonded organic framework biomimetic entrapment allowing non-native biocatalytic activity in enzyme. *Nat. Commun.* **13**, 4816 (2022).
65. Li, Y. et al. A microporous hydrogen bonded organic framework for highly selective separation of carbon dioxide over acetylene. *Angew. Chem. Int. Ed.* **62**, e202311419 (2023).
66. Cheng, Z. et al. Hydrogen-bonded organic framework to upgrade cycling stability and rate capability of Li-$CO_2$ batteries. *Angew. Chem. Int. Ed.* **62**, e202311480 (2023).
67. Huang, J. et al. A microporous hydrogen-bonded organic framework based on hydrogen-bonding tetramers for efficient Xe/Kr separation. *Angew. Chem. Int. Ed.* **62**, e202315987 (2023).
68. Wang, B. et al. Microporous hydrogen-bonded organic framework for highly efficient turn-up fluorescent sensing of aniline. *J. Am. Chem. Soc.* **142**, 12478–12485 (2020).
69. Bassanetti, I. et al. Flexible porous molecular materials responsive to $CO_2$, $CH_4$ and Xe stimuli. *J. Mater. Chem. A.* **6**, 14231–14239 (2018).
70. Ward, M.D. Design of crystalline molecular networks with charge-assisted hydrogen bonds. *Chem. Commun.* **47**, 5838–5842 (2005).
71. Slavney, A. H. et al. Liquid and glass phases of an alkylguanidinium sulfonate hydrogen-bonded organic framework. *J. Am. Chem. Soc.* **144**, 11064–11068 (2022).
72. Yang, X. et al. Solution-processed hydrogen-bonded organic framework nanofilms for high-performance resistive memory devices. *Adv. Mater.* **35**, e2305344 (2023).
73. Bosnidou, A. E. & Muniz, K. Intermolecular radical Csp3-H amination under iodine catalysis. *Angew. Chem. Int. Ed.* **58**, 7485–7489 (2019).
74. Cai, S., An, Z. & Huang, W. Recent advances in iuminescent hydrogen-bonded organic frameworks: structures, photophysical properties, applications. *Adv. Funct. Mater.* **32**, 2207145 (2022).
75. Shi, Y. et al. Multiple yet switchable hydrogen-bonded organic frameworks with white-light emission. *Nat. Commun.* **13**, 1882 (2022).
76. Chen, Q. et al. Tunable fluorescence in two-component hydrogen-bonded organic frameworks based on energy transfer. *ACS Appl. Mater. Interfaces* **14**, 24509–24517 (2022).
77. Tholen, P. et al. Tuning structural and optical properties of porphyrin-based hydrogen-bonded organic frameworks by metal insertion. *Small* **18**, e2204578 (2022).


## Acknowledgements

We acknowledge the National Natural Science Fund for Excellent Young Scholars (No. 21922604, G.Y.), the National Natural Science Foundation of China (No. 22376117, G.Y.; No. 22206105, X.D.), and Tsinghua University Initiative Scientific Research Program (G.Y.) for the financial support of this work.

## Author contributions

X.D. and G.Y. designed the experiment and synthesized crystalline materials. X.D. and G.Y. conducted the experiment and wrote the article. J.C. provided valuable suggestions for the study.

## Competing interests

The authors declare no competing interests.

## Additional information

**Supplementary information** The online version contains supplementary material available at https://doi.org/10.1038/s41467-024-47058-1.

**Correspondence** and requests for materials should be addressed to Xiaojun Ding or Gang Ye.

**Peer review information** *Nature Communications* thanks Antonio Fernández, Zhangjing Zhang and the other, anonymous, reviewer(s) for their contribution to the peer review of this work. A peer review file is available.